This is a post-peer-review, pre-copyedit version of an article published in Journal of the Brazilian Society of Mechanical Sciences and Engineering. The final authenticated version is available online at: https://doi.org/10.1007/s40430-022-03468-0".

3D printing of trabecular bone-mimetic structures by vat photopolymerization of bovine hydroxyapatite as a potential candidate for scaffolds.

Rogério Erbereli[a*], Italo Leite de Camargo[a,b], Mateus Mota Morais[a] and Carlos Alberto Fortulan[a]

[a] Mechanical Engineering Department - São Carlos School of Engineering, University of São Paulo – USP, 13566-590, São Carlos, SP, Brazil.

[b] Federal Institute of Education, Science and Technology of São Paulo – IFSP, 01109-970, Itaquaquecetuba, SP, Brazil.

[*] Correspondence e-mail: rogerio.erbereli@usp.br

ORCID: Rogério Erbereli: 0000-0003-0753-8172

Italo Leite de Camargo: 0000-0001-8329-6799

Mateus Mota Morais: 0000-0002-5318-8129

Carlos Alberto Fortulan: 0000-0002-2259-9910

Accepted manuscript published at Journal of the Brazilian Society of Mechanical Sciences and Engineering

DOI: https://doi.org/10.1007/s40430-022-03468-0

Abstract

The growing demand for bone-repairing applications has boosted the research for functional biomaterials, their processing, and their conformation into bone scaffolds with controlled morphology and dimensions.

However, it is still challenging and expensive to manufacture bioceramic scaffolds with complex morphology and tailored porosity. This paper presents the processing of low-cost hydroxyapatite from widely available bovine bones and the development of mimetic bone structures by vat photopolymerization additive manufacturing. First, bovine bones were processed to become reactive bioceramic hydroxyapatite through calcination and milling; a route called ceramization that eliminates any biological risk. Second, hydroxyapatite suspensions were developed with high solid loading (40 vol%), excellent stability (> 30 days) and low viscosity (< 200 mPa.s). Finally, a bovine trabecular bone was microCT scanned and replicated as mimetic bones through additive manufacturing vat photopolymerization using the obtained hydroxyapatite suspension. The printed scaffolds showed adequate mechanical resistance, similar to natural bone, verified by mechanical tests and finite element simulation. Conclusively, the presented methodology results in a promising combination of morphology, mechanical resistance and biocompatibility suited for bone scaffolds, using low-cost bovine-derived hydroxyapatite. Also, the described processing has a high potential for tissue engineering of customized/complex scaffolds for implants.

Keywords: bovine hydroxyapatite, additive manufacturing, 3D printing, scaffolds, photopolymerization.

1. Introduction

The main destination of porous bone scaffolds is repairing damaged bones; however, scaffolds are not intended to replace bone permanently but rather to provide mechanical support for the growth of new natural bone. Therefore, an ideal scaffold should: promote intraosseous formation and vascularization by stimulating the proliferation of new cells within the porosity of the scaffold (osteointegration); support the mechanical loads while the bone is regenerating [1–7]; allow the flow of blood and body fluids (osteoconductivity) [7–10]; and be bioabsorbable after new bone formation. Notably, bone scaffolds must have high porosity with controlled pore morphology, size, distribution and interconnectivity [1,11–13]. Therefore, there has been intense research on biocompatible materials and manufacturing routes to meet all these requirements.

Additive manufacturing (AM) has stood out among the scaffold fabrication technics due to the possibility of producing highly complex and customizable ceramic parts in small series without the high costs of molds [8,14]. Vat photopolymerization (VP) is an AM process that can produce tiny ceramic

structures with outstanding dimensional precision (≈ 50μm) [15–17]. Thus, it has emerged as one of the best AM technologies for the fabrication of bioceramic scaffolds [18–33]. In this process, the bioceramic powder is mixed with a liquid photopolymer and is solidified in a vat, layer by layer, by light polymerization. Then the composite body goes through a heat treatment in which the organics are eliminated (debinding), and the ceramic is sintered [34–36].

However, producing parts using VP with controlled porosity, precise dimension and adequate mechanical strength is challenging. These characteristics are highly dependent on the properties of the ceramic suspensions, especially solid loading, rheology and curing behavior [37]. Therefore, the preparation of these ceramic slurries is critical and requires further studies and optimization, especially when using materials that were not previously applied to the VP process.

Selecting the appropriate raw materials is an essential factor in the success of ceramic additive manufacturing. For instance, hydroxyapatite (HA) is one of the most popular materials associated with the fabrication of bone tissue because it promotes osseointegration [38]. In recent years, many researchers have studied the feasibility of producing HA bone scaffolds by VP [8,14,20,22–24,28–32,35,36,39–42]. However, they all use commercial synthetic HA powders, which are expensive raw materials. An alternative to circumvent the cost limitation is the use of bovine-derived hydroxyapatite. The use of this bovine-derived material is highlighted in research because it is similar to human bone, exhibiting excellent biocompatibility and osteoconductivity [43–46].

This article presents the fabrication of high-performance, low-cost bioceramic parts by VP using bovine-derived hydroxyapatite, with full material traceability for the first time. Furthermore, the processing of the bovine bones into reactive HA submicrometric powder is fully described. The processed bovine HA was used to prepare solvent-free photosensitive suspensions with high solid loading and low viscosity. Finally, scaffolds that mimic trabecular bone were successfully printed in a homemade VP 3D printer using the HA photosensitive suspensions.

2. Materials and methods

Hydroxyapatite (HA) powders were obtained from two different bovine breeds (Nelore and Canchim), according to Erbereli [47]. It is noteworthy that the HA produced from both breeds have similar structural and architectural characteristics [47]. The bone was broken into small pieces, calcined (either at 900 or 1300°C), and submitted to manual crushing in a mortar and pistil. The resulting powder

was ball-milled in an alcoholic solution for 24 hours, followed by vibratory milling for 72 hours. During the milling process, a sample of the suspension was collected after every 24 hours and characterized in terms of particle size by SediGraph III Plus Particle Size Analyzer (Micromeritics). The measurement principle was X-Ray monitored gravity sedimentation, and the calculation method was the Stokes sedimentation and Beer's law of extinction.

The bovine-derived HA powders produced under different conditions (after milling, calcined at 900°C, calcined at 1300°C, and sintered at 1300°C) were characterized by X-ray diffraction and compared with a commercial hydroxyapatite powder (Sigma Aldrich - Fluka - batch: 1231469 - CAS No.: 1306-06-5), a material that meets the ASTM 1185 – 03 (Standard Specification for Hydroxyapatite Composition for Surgical Implants) [48]. The diffraction tests were performed for each condition in a Shimadzu XDR-7000 equipment with 40 kV and 30 mA, CuK-α radiation (wavelength $\lambda = 1.54056$Å). The θ - 2θ analysis were scanned from 5 to 90 ° with a step 0.02° every 0.6 seconds.

The 3D bone digital model, later used for additive manufacturing and finite element simulation, was obtained from a piece of a posterior metatarsal bovine bone (Figure 1a) with cortical and trabecular portions using X-Ray microtomography (SkyScan 1272, Bruker, with XIMEA camera xiRAY16). A slice was acquired every 0.067742 seconds, resulting in a total of 1240 slices, each with 1240 x 2176 pixels (width and height, respectively). Next, the grayscale slices images were binarized, converted to a solid surface STL file (Figure 1b). Finally, a cube of 1 cm^3 of the trabecular section was generated through a Boolean cut operation (Figure 1c).

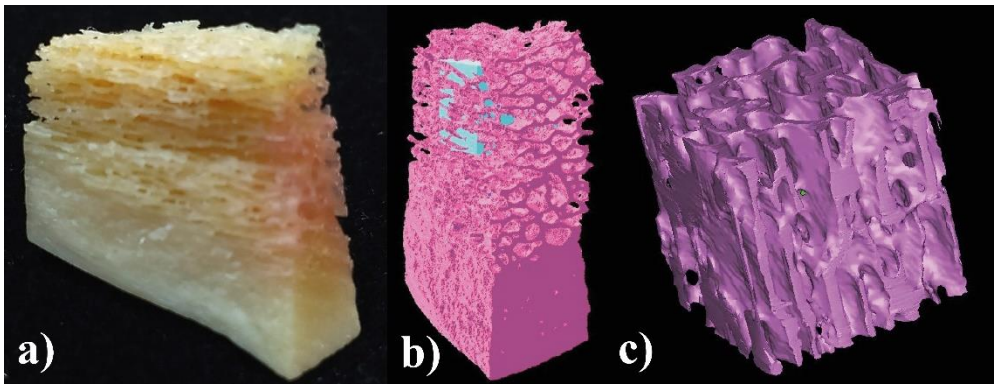

Figure 1 – 3D model acquisition. a) metatarsal bovine piece. b) Scanned 3D model with a highlighted cube (green) for Boolean cutting. c) Resulting cube from trabecular portion (model).

Three ceramic suspensions were developed using variable solid loadings (30, 35 and 40% vol) of bovine-derived HA powder calcined at 1300°C. Poly (ethylene glycol) diacrylate (average Mn250 - Sigma Aldrich) was used as monomer and Triton X-100 (Sigma Aldrich, USA) as dispersant (3wt % of the ceramic powder). The suspensions were ball milled for 24 hours to obtain a homogeneous suspension, as suggested by Camargo [49]. The rheological behavior of the three slurries was characterized using a rotational viscometer model DV2T extra (Brookfield, Canada) at room temperature (between 23 and 25°C). The colloidal suspension stability of the slurries was verified by a sedimentation test, where 10 ml of each suspension were poured into graduated tubes, as described in other studies related to ceramic photosensitive suspensions [49–54]. The measuring tubes were kept undisturbed for 30 days, and the fraction of the sedimentation volume was recorded as a function of time.

After analyzing the rheology and stability tests, the 40 vol% suspension was selected for 3D printing. The photoinitiator Phenylbis (2,4,6-trimethylbenzoyl) phosphine oxide (PPO, Sigma Aldrich, USA) was added to the slurry in the amount of 2 wt % of the monomer, according to references that suggest the use of 0.5 to 3 wt% of photoinitiator [17,55–57]. The suspension was again processed in a ball mill for more 24 hours for proper mixing of the photoinitiator.

Samples of the 3D model of the trabecular bone were additively manufactured on a home-built Top-Down DLP printer described by Camargo [58] using the 40 vol% bovine-derived suspension. This printer uses a light projector with a mercury vapor lamp that provides 0.5 mW/cm^2 of useful irradiance at wavelengths between 380 and 420 nm [59]. Different exposure energies per layer (5, 7.5 and 10 mJ/cm^2) were tested to find adequate exposure energy to manufacture parts with 100 μm thick layers.

In order to have a reference to evaluate the mechanical resistance of the printed parts, ten cylinders of bovine-derived HA were produced by isostatic compaction. First, the HA was mixed with the binder polyvinyl butyral (PVB) (1.2 wt % of the HA powder). The PVB was previously dissolved in isopropyl alcohol in the proportion 1:10 vol. Next, the slurry was mixed in a ball mill for 2h, followed by drying using a hot air blower. The dried powder was sieved with an 80# mesh (180 μm). Then, ten cylinders, each with 0.63±0.01 g, were uniaxially compacted with a pneumatic press with a 6 mm diameter mold. Finally, the preformed cylinders were evacuated and sealed inside a latex elastomer and isostatically compacted at 190 MPa.

The debinding and sintering of the printed parts were performed in a box furnace (Blue M, Lindberg) in an air environment, using the heating program shown in Figure 2. The heating rate was

reduced in the thermal degradation temperature range of the monomer (major organic component) [60] to minimize cracks [61,62]. The compacted cylinders were also sintered at 1300°C for 2h. The 3D printed bones and the compacted cylinders were measured with a digital caliper. The density of 3D printed parts was measured based on Archimedes' principle, following the ASTM C373-18 standard [63] using an analytical balance with a resolution of 0.01 mg (AUW220D, Shimadzu).

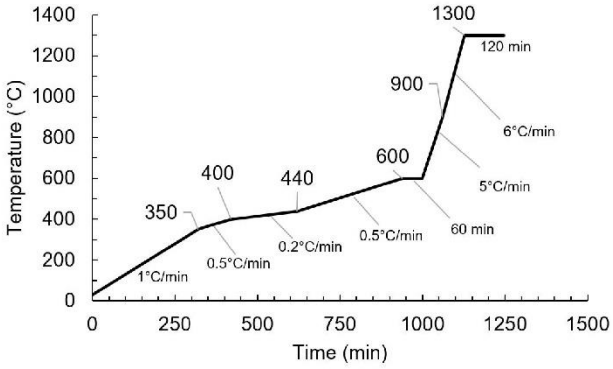

Figure 2 – Sintering curve.

Mechanical compression tests were carried out in a universal electronic test machine MTS® Model 370.02 Bionix Servohydraulic Load Frame, 15 kN load cell, with a speed of 0.1mm/m being applied for the tests. Ten compacted cylinders and five 3D printed mimetic bones were tested. The projected area of the sintered bone scaffolds was approximately 72 mm^2. The tests were based on the ASTM C1424 − 15 [64].

The compaction test of the printed samples was reproduced using the finite element method (FEM) in Ansys Mechanical. Before the simulation, the STL file of the trabecular bone was edited using the free software Autodesk MeshMixer. The following modifications were performed on the STL file: Scaling the file to match the sintered 3D printed part dimensions (7.07 x 8.25 x 8.55 mm), removing mesh defects (non-connected regions, non-manifold vertexes, mesh holes); cutting a slice (< 0.25 mm) of the faces to make them flatter to apply the loads; removing very thin material sections that would be highly costly to simulate and would not considerable contribute to material stiffness; performing adaptative remeshing to reduce archive size and regularize surface triangles. The edited STL file was imported to Ansys Space Claim as a connected faceted body. The file was automatically fixed for errors and converted to a solid with merged faces before exporting to Ansys Mechanical.

The HA properties adopted for the simulation were obtained from [65] (density 3100 kg/m^3, Young's modulus 100 GPa, Poison's ratio 0.28). The material was assumed linear elastic and isotropic. After importing the bone geometry, the solid was meshed with second-order tetrahedrons (Tet10) using the patch conforming method with automatic adaptative size resolution 6. The resulting mesh had 493,867 elements and 836,718 nodes (average element length of 0.08 mm). The bottom of the digital bone was constrained with frictionless support (x = 0) and one of the edges was fixed to avoid solid-body motion. In the first simulation step, the load was applied by displacing the upper face by -1.3132 µm in the x-direction. This displacement corresponds to the application of 90 N in the upper face, which was the average force necessary for the partial breakage of the printed bones in the mechanical test. A second simulation step was performed with a displacement of -5.2529 µm in the upper face, corresponding to a force of 360 N, which was the ultimate load that caused the printed samples to collapse. Figure 3 depicts the meshed solid with a schematic representation of the applied load and boundary conditions. The simulation was performed with the iterative solver and computed large deflections.

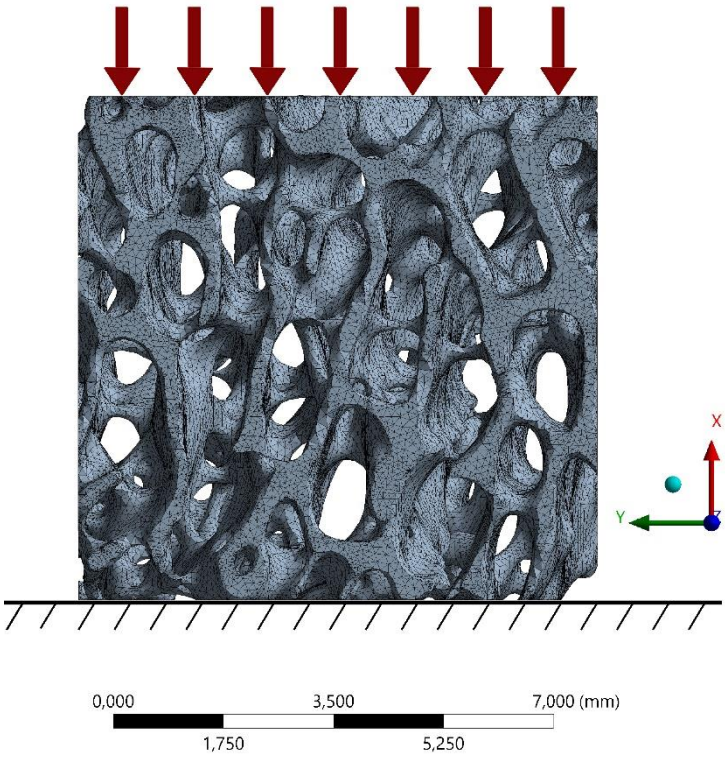

Figure 3 – FEM mesh of the model bone with a schematic representation of the boundary conditions and loads.

3. Results

Figure 4 shows the evolution of the milling process. Although larger particles result in lower suspension viscosity, fine particles are more reactive than larger ones during sintering and may provide parts with better mechanical properties. The usual range of mean particle size for studies related to ceramics vat photopolymerization is up to 0.5 microns [37]. Therefore, the powder submitted to 72 hours of vibratory milling was chosen for providing a mean particle size closer to this value.

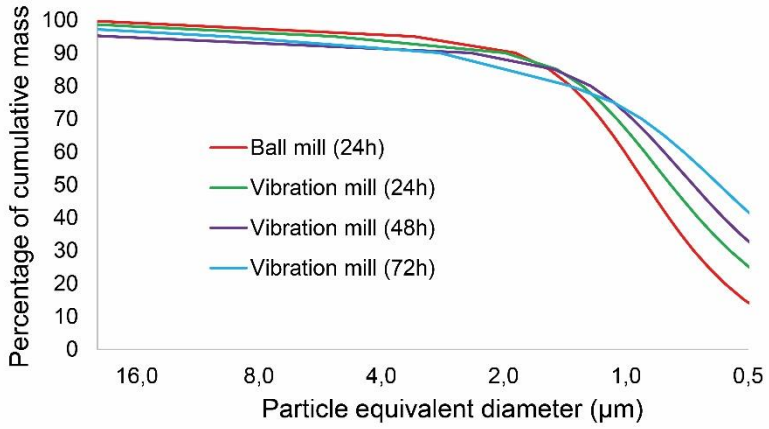

Figure 4 - Grinding curves.

Figure 5 shows the diffractograms of different bovine-derived HA powders (commercial, after milling, calcined at 900°C, and 1300°C, and from a 3D printed part sintered at 1300°C). The comparison indicates high similarity between the diffractograms of the commercial powder and the calcined HA at 1300°C. On the contrary, the milled powder and calcined bone at 900°C presented less crystallinity. Hence, the calcination temperature was chosen to be 1300°C instead of 900°C. Furthermore, the sintered part at 1300°C also showed high similarity with the commercial powder. It demonstrates that all the photocurable resin used in the 3D printing process is eliminated with the heat treatment. Also, the sintering operation does not change the stabilization of the HA phase, which could lead to its transformation into tricalcium phosphate. Finally, the sintered HA appears to have higher crystallinity due to the greater intensity of the peaks and narrowing of the bases in the diffractogram.

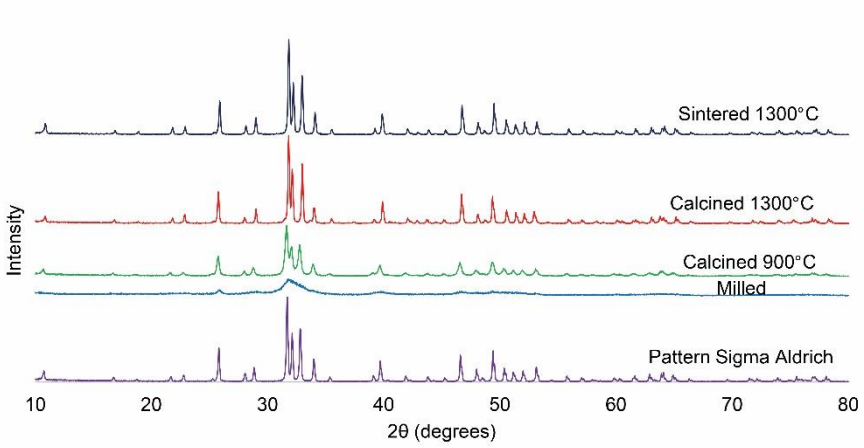

Figure 5 - Comparative diffractograms of hydroxyapatite.

The influence of solid loading on the rheological behavior of the ceramic suspension can be seen in Figure 6a. It can be noticed that the viscosity increases with increasing solid loading. All the suspensions showed shear-thickening behavior (characterized by a viscosity increase with increasing shear rate), which was accentuated for higher solid loadings. Moreover, all the suspensions presented viscosity lower than 200 mPa.s in all measured shear rates, which was suitable for the 3D printer recoating system [15,66,67]. Interestingly, the achieved viscosity is considerably smaller than other studies on bioceramics suspensions for vat photopolymerization [23,39,68,69]. This good result was achieved due to adequate choice of monomer and dispersant, as well as the control of the particle size of the bioceramic powder.

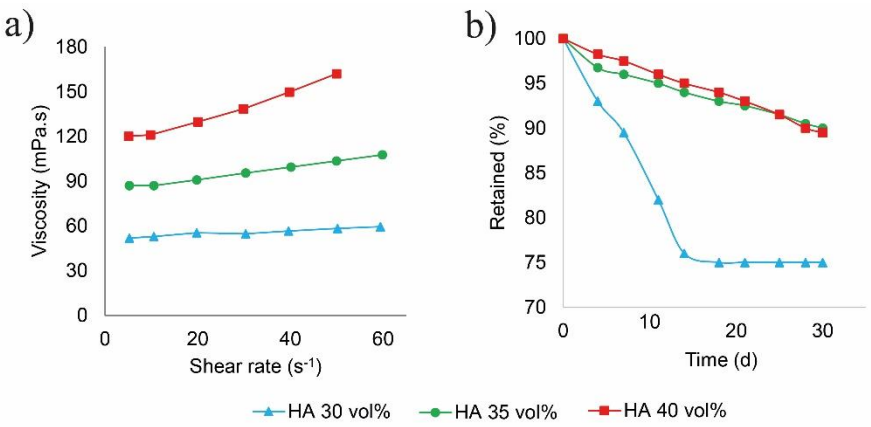

Figure 6 – Hydroxyapatite suspensions with different solid load characterization. a) Viscosity curves. b) Sedimentation tests.

It can be seen from Figure 6b that the solids loading of 30 vol% of HA showed a higher segregation rate, reaching a total of 25% during the test. On the other hand, samples with loads of 35 and 40 vol% loading showed similar segregation behavior over the 30 days of testing with total segregation of only 10% and negligible sedimentation in the first days of the test, thus being suitable for the process. As a good practice, it is indicated that the suspension should always be stirred before use. Considering its adequate rheological behavior and stability demonstrated in the tests, the 40 vol% solid loading ceramic slurry was used to manufacture the mimetic bones.

Concerning the printing parameters, an exposure energy of 5 mJ / cm^2 resulted in the delamination of the layers during printing. Thus, it was impossible to complete the fabrication. Similarly, printed parts with an exposure energy of 7.5 mJ / cm^2 also presented delamination. On the other hand, the tests carried out with an exposure energy of 10 mJ / cm^2 presented no delamination problems in any of the additively manufactured parts. Figure 7 shows the 3D printed mimetic trabecular bones from model, using the best condition found: ceramic paste with 40 vol% HA load and exposure energy of 10 mJ / cm^2. Figure 8 presents a detailed view of the layers observed by optical microscopy, highlighting the homogeneous layers and no apparent delamination problems. The richness of detail in the printed parts was possible due to the use of high-resolution micro-CT to generate the 3D model and the optimization of the printing conditions.

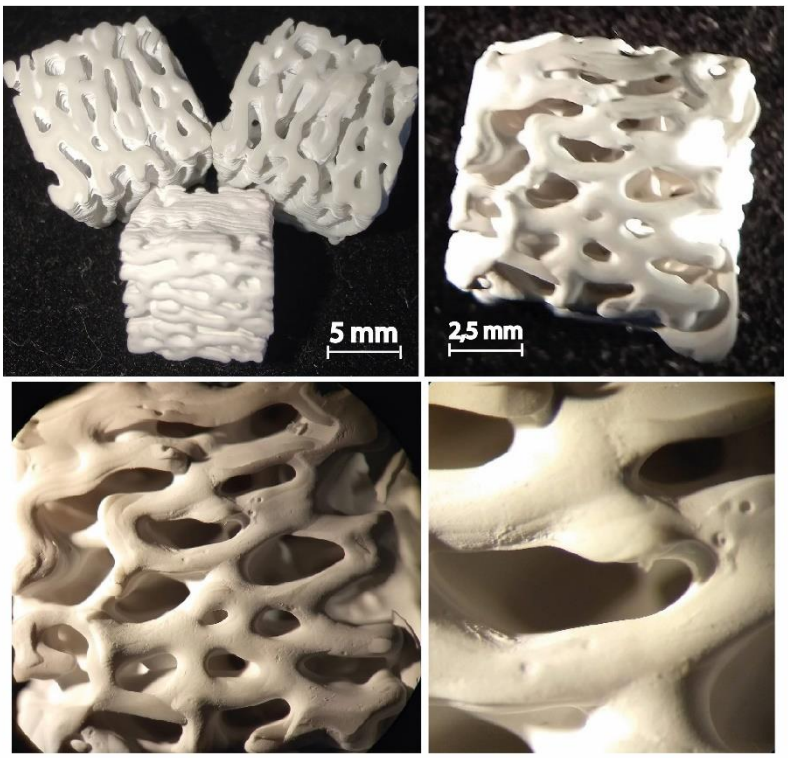

Figure 7 – Sintered 3D printed mimetic trabecular from model bone structure, using a ceramic slurry with 40 %vol of HA loading and exposure energy of 10 mJ/cm^2.

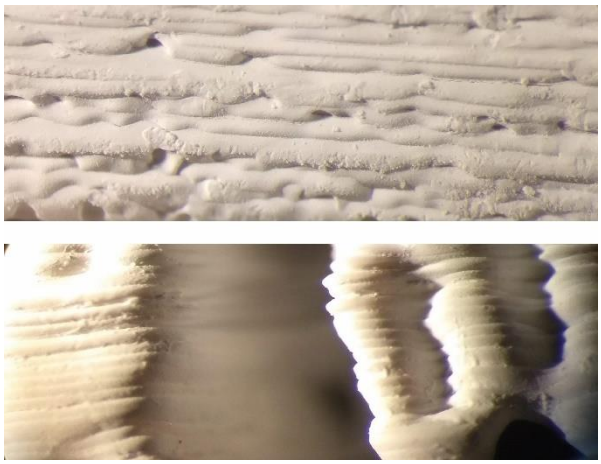

Figure 8 – Printing layers of specimens.

After sintering, the dimensions of the compacted cylinders were: 9.57±0.11 mm in height and 5.16±0.01 mm in diameter. The compression tests of the cylindrical bodies presented average rupture stress of 280±60 MPa, which agrees with literature data for hydroxyapatite [65]. After sintering, the 3D printed mimetic bones presented the following dimensions: 7.07±0.19 x 8.25±0.12 x 8.55±0.07 mm, with a relative density of about 82%, a value slightly lower than related by other studies [70,71]. However, this

value could be improved by increasing the solid loading, sintering temperature, or sintering dwell time, which may be the subject of future studies.

The 3D-printed mimetic bones showed a more complex behavior than the compacted cylinders during the mechanical compression tests. Because the printed parts have several small trabecular connections, the stress distribution is non-uniform and partial rupture occurs at different stages before the ultimate fracture of the mimetic bone. The first significant partial rupture was detected with 90±50 N and the ultimate rupture load was 360 ± 104 N. Considering the projected area of the scaffold, this load corresponds to an apparent ultimate stress of 5.00±1.45 MPa, as presented in Table 1. Remarkably, the resistance of the 3D printed mimetic bone is similar to natural bone [72], highlighting its potential applicability as bone scaffold. Despite the morphology of these 3D printed mimetic bones being more complex than other scaffolds found in literature, they presented good mechanical resistance, similar or even higher to other reported results [22,23,27,29,31,73].

Concerning the FEM simulation, Table 1 summarizes its main results. Figure 9 shows the stresses in the loading condition corresponding to the first partial rupture that occurred in the mechanical test (90 N applied). As expected, the stress distribution was non-uniform. Although the average stress was low, 8.27 MPa, some highly loaded regions had stresses as high as 263.6 MPa, only 5% lower than the ultimate stress found in the compacted cylinders (280 MPa). Therefore, it can be concluded that despite the layered morphology created by the additive manufacturing process, the intrinsic resistance of the material was retained significantly, evidencing the quality of the manufacturing process. Furthermore, even when the ultimate load was applied (360 N), the average stress was low, 33 MPa, evidencing that the rupture of the material was caused by localized fracture at stress concentrations.

Table 1 – Finite element simulation results.

	Load (N) (N)	Average Stress (MPa)	Maximum stress (MPa)
First peak	90.00	8.27	263.56
Ultimate peak	359.56	33.07	1053.9

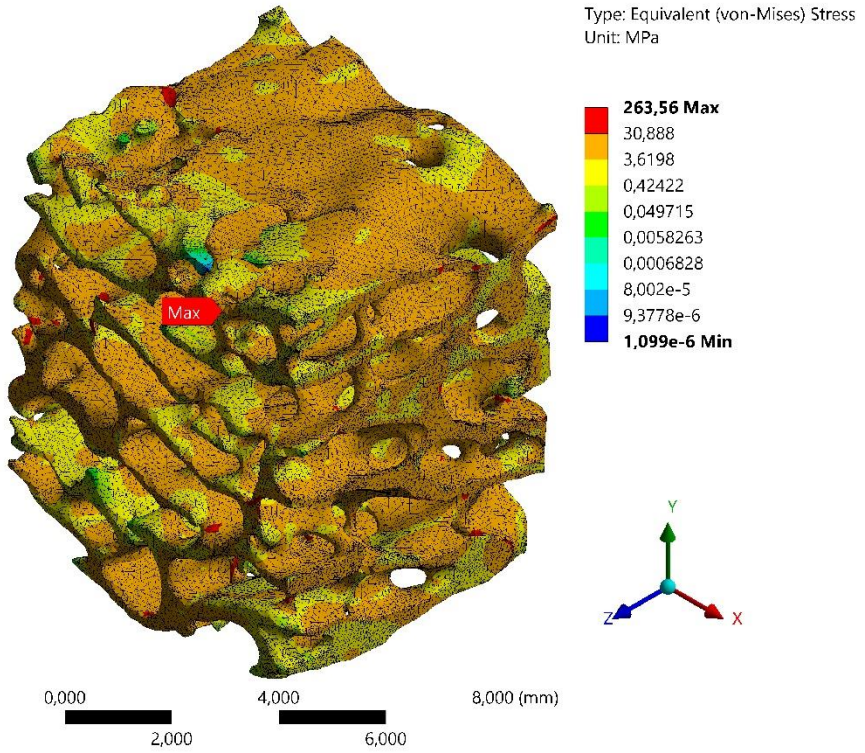

Figure 9 – Equivalent stress results of the finite element simulation of the 3D printed mimetic trabecular bone submitted to 90 N compression.

4. Conclusion

The processing methodology for bovine-derived hydroxyapatite with traceability, through calcination and grinding by ball and vibratory mills, proved to be an efficient way in obtaining submicrometric reactive powders. The produced powders have proper particle size for the development of vat photopolymerization. Also, the processed bovine-derived hydroxyapatite calcined at 1300 °C proved to have high crystallinity and similarity with commercial powders.

The bovine-derived HA suspension with 40 vol% loading proved to have suitable stability and rheological behavior, with a viscosity below 200 mPa.s over the entire shear rate range test. As a result, the HA suspension was successfully used to manufacture hydroxyapatite parts. Among the different exposure energies tested, 10 mJ/cm^2 showed satisfactory results, resulting in parts without delamination and with dimensional accuracy, reproducing the complex trabecular morphology and porosity.

The mechanical resistance of the 3D printed parts was proper for scaffold applications, confirmed both by the mechanical tests and the finite element simulation. Furthermore, the resistance

calculated by finite element simulation (263 MPa) was only 5% lower than the compacted hydroxyapatite samples, highlighting the excellent quality of the proposed manufacturing route.

The use of hydroxyapatite of bovine origin, an economical and widely available material, proved suitable for the additive manufacturing of scaffolds and mimetic bones. The feasibility of using similar parts in personalized bone implants, especially their biocompatibility and osteointegration, may be the subject of future studies.

5. Conflict of interest and Acknowledgement

The authors declare no conflicts of interest. The present work was carried out with the support of the Coordination of Improvement of Superior - Brazil (CAPES) - Financing Code 001 and the São Paulo Research Foundation (FAPESP), grant #2020/16012-1.

6. References

[1] Miculescu F, Maidaniuc A, Miculescu M, Dan Batalu N, Catalin Ciocoiu R, Voicu ŞI, et al. Synthesis and Characterization of Jellified Composites from Bovine Bone-Derived Hydroxyapatite and Starch as Precursors for Robocasting. ACS Omega 2018;3:1338–49. doi:10.1021/acsomega.7b01855.

[2] Vijayavenkataraman S, Zhang L, Zhang S, Fuh JYH, Lu WF. Triply periodic minimal surfaces sheet scaffolds for tissue engineering applications: An optimization approach toward biomimetic scaffold design. ACS Appl Bio Mater 2018;1:259–69. doi:10.1021/acsabm.8b00052.

[3] Song JE, Tripathy N, Lee DH, Park JH, Khang G. Quercetin Inlaid Silk Fibroin/Hydroxyapatite Scaffold Promotes Enhanced Osteogenesis. ACS Appl Mater Interfaces 2018;10:32955–64. doi:10.1021/acsami.8b08119.

[4] Eltom A, Zhong G, Muhammad A. Scaffold Techniques and Designs in Tissue Engineering Functions and Purposes: A Review. Adv Mater Sci Eng 2019;2019. doi:10.1155/2019/3429527.

[5] Cheng A, Schwartz Z, Kahn A, Li X, Shao Z, Sun M, et al. Advances in Porous Scaffold Design for Bone and Cartilage Tissue Engineering and Regeneration. Tissue Eng - Part B Rev

2019;25:14–29. doi:10.1089/ten.teb.2018.0119.

[6] Mondal S, Nguyen TP, Pham VH, Hoang G, Manivasagan P, Kim MH, et al. Hydroxyapatite nano bioceramics optimized 3D printed poly lactic acid scaffold for bone tissue engineering application. Ceram Int 2020;46:3443–55. doi:10.1016/j.ceramint.2019.10.057.

[7] Mondal S, Pal U, Dey A. Natural origin hydroxyapatite scaffold as potential bone tissue engineering substitute. Ceram Int 2016;42:18338–46. doi:10.1016/j.ceramint.2016.08.165.

[8] Kumar A, Kargozar S, Baino F, Han SS. Additive Manufacturing Methods for Producing Hydroxyapatite and Hydroxyapatite-Based Composite Scaffolds: A Review. Front Mater 2019;6. doi:10.3389/fmats.2019.00313.

[9] Gul H, Khan M, Khan AS. 3 - Bioceramics: types and clinical applications. Elsevier Ltd; 2020. doi:https://doi.org/10.1016/B978-0-08-102834-6.00003-3.

[10] Amin AMM, Ewais EMM. Bioceramic Scaffolds. Scaffolds Tissue Eng - Mater Technol Clin Appl 2017. doi:10.5772/intechopen.70194.

[11] Shanmugam K, Sahadevan R. Bioceramics-An introductory overview. Elsevier Ltd.; 2018. doi:10.1016/B978-0-08-102203-0.00001-9.

[12] Shao H, He J, Lin T, Zhang Z, Zhang Y, Liu S. 3D gel-printing of hydroxyapatite scaffold for bone tissue engineering. Ceram Int 2019;45:1163–70. doi:10.1016/j.ceramint.2018.09.300.

[13] Tang D, Tare RS, Yang LY, Williams DF, Ou KL, Oreffo ROC. Biofabrication of bone tissue: Approaches, challenges and translation for bone regeneration. Biomaterials 2016;83:363–82. doi:10.1016/j.biomaterials.2016.01.024.

[14] Ferrage L, Bertrand G, Lenormand P, Grossin D, Ben-Nissan B. A review of the additive manufacturing (3DP) of bioceramics: Alumina, zirconia (PSZ) and hydroxyapatite. J Aust Ceram Soc 2017;53:11–20. doi:10.1007/s41779-016-0003-9.

[15] Schwentenwein M, Homa J. Additive manufacturing of dense alumina ceramics. Int J Appl Ceram Technol 2015;12:1–7. doi:10.1111/ijac.12319.

[16] Zhang K, He R, Ding G, Feng C, Song W, Fang D. Digital light processing of 3Y-TZP strengthened ZrO2 ceramics. Mater Sci Eng A 2020;774:138768. doi:10.1016/j.msea.2019.138768.

[17] Santoliquido O, Colombo P, Ortona A. Additive Manufacturing of ceramic components by Digital Light Processing: A comparison between the “bottom-up” and the “top-down”

approaches. J Eur Ceram Soc 2019;39:2140–8. doi:10.1016/j.jeurceramsoc.2019.01.044.

[18] Wang JC. A novel fabrication method of high strength alumina ceramic parts based on solvent-based slurry stereolithography and sintering. Int J Precis Eng Manuf 2013;14:485–91. doi:10.1007/s12541-013-0065-3.

[19] Layani M, Wang X, Magdassi S. Novel Materials for 3D Printing by Photopolymerization. Adv Mater 2018;30:1–7. doi:10.1002/adma.201706344.

[20] Li X, Yuan Y, Liu L, Leung YS, Chen Y, Guo Y, et al. 3D printing of hydroxyapatite/tricalcium phosphate scaffold with hierarchical porous structure for bone regeneration. Bio-Design Manuf 2020;3:15–29. doi:10.1007/s42242-019-00056-5.

[21] Elsayed H, Picicco M, Ferroni L, Gardin C, Zavan B, Bernardo E. Novel bioceramics from digital light processing of calcite/acrylate blends and low temperature pyrolysis. Ceram Int 2020;46:17140–5. doi:10.1016/j.ceramint.2020.03.277.

[22] Du Y, Hu T, You J, Ye Y, Zhang B, Bao B, et al. Study of falling-down-type DLP 3D printing technology for high-resolution hydroxyapatite scaffolds. Int J Appl Ceram Technol 2021:1–13. doi:10.1111/ijac.13915.

[23] Zeng Y, Yan Y, Yan H, Liu C, Li P, Dong P, et al. 3D printing of hydroxyapatite scaffolds with good mechanical and biocompatible properties by digital light processing. J Mater Sci 2018;53:6291–301. doi:10.1007/s10853-018-1992-2.

[24] Wang Z, Huang C, Wang J, Zou B. Development of a novel aqueous hydroxyapatite suspension for stereolithography applied to bone tissue engineering. Ceram Int 2019;45:3902–9. doi:10.1016/j.ceramint.2018.11.063.

[25] Wen Y, Xun S, Haoye M, Baichuan S, Peng C, Xuejian L, et al. 3D printed porous ceramic scaffolds for bone tissue engineering: A review. Biomater Sci 2017;5:1690–8. doi:10.1039/c7bm00315c.

[26] Van hede D, Liang B, Anania S, Barzegari M, Verlée B, Nolens G, et al. 3D-Printed Synthetic Hydroxyapatite Scaffold With In Silico Optimized Macrostructure Enhances Bone Formation In Vivo. Adv Funct Mater 2021;2105002:2105002. doi:10.1002/adfm.202105002.

[27] Kim JW, Yang BE, Hong SJ, Choi HG, Byeon SJ, Lim HK, et al. Bone regeneration capability of 3D printed ceramic scaffolds. Int J Mol Sci 2020;21:1–13. doi:10.3390/ijms21144837.

[28] Wang Z, Huang C, Wang J, Zou B, Abbas CA, Wang X. Design and Characterization of

Hydroxyapatite Scaffolds Fabricated by Stereolithography for Bone Tissue Engineering Application. Procedia CIRP 2020;89:170–5. doi:10.1016/j.procir.2020.05.138.

[29] Baino F, Magnaterra G, Fiume E, Schiavi A, Tofan LP, Schwentenwein M, et al. Digital light processing stereolithography of hydroxyapatite scaffolds with bone-like architecture, permeability, and mechanical properties. J Am Ceram Soc 2021:1–10. doi:10.1111/jace.17843.

[30] Tang Q, Li X, Lai C, Li L, Wu H, Wang Y, et al. Fabrication of a hydroxyapatite-PDMS microfluidic chip for bone-related cell culture and drug screening. Bioact Mater 2021;6:169–78. doi:10.1016/j.bioactmat.2020.07.016.

[31] Cho YS, Yang S, Choi E, Kim KH, Gwak SJ. Fabrication of a porous hydroxyapatite scaffold with enhanced human osteoblast-like cell response via digital light processing system and biomimetic mineralization. Ceram Int 2021;47:35134–43. doi:10.1016/j.ceramint.2021.09.056.

[32] Feng C, Zhang K, He R, Ding G, Xia M, Jin X, et al. Additive manufacturing of hydroxyapatite bioceramic scaffolds: Dispersion, digital light processing, sintering, mechanical properties, and biocompatibility. J Adv Ceram 2020;9:360–73. doi:10.1007/s40145-020-0375-8.

[33] Le Guéhennec L, Van hede D, Plougonven E, Nolens G, Verlée B, De Pauw MC, et al. In vitro and in vivo biocompatibility of calcium-phosphate scaffolds three-dimensional printed by stereolithography for bone regeneration. J Biomed Mater Res - Part A 2020;108:412–25. doi:10.1002/jbm.a.36823.

[34] Milazzo M, Contessi Negrini N, Scialla S, Marelli B, Farè S, Danti S, et al. Additive Manufacturing Approaches for Hydroxyapatite-Reinforced Composites. Adv Funct Mater 2019;29:1–26. doi:10.1002/adfm.201903055.

[35] Tufail A, Schmidt F, Maqbool M. Three-dimensional printing of hydroxyapatite. Elsevier Ltd; 2020. doi:10.1016/b978-0-08-102834-6.00015-x.

[36] Liu Z, Liang H, Shi T, Xie D, Chen R, Han X, et al. Additive manufacturing of hydroxyapatite bone scaffolds via digital light processing and in vitro compatibility. Ceram Int 2019;45:11079–86. doi:10.1016/j.ceramint.2019.02.195.

[37] Camargo IL de C, Morais MM, Fortulan CA, Branciforti MC. A review on the rheological behavior and formulations of ceramic suspensions for vat photopolymerization. Ceram Int 2021. doi:10.1016/j.ceramint.2021.01.031.

[38] Parkhomey O, Pinchuk N, Sych O, Tomila T, Kuda O, Tovstonoh H, et al. Effect of particle size

of starting materials on the structure and properties of biogenic hydroxyapatite/glass composites. Process Appl Ceram 2016;10:1–8. doi:10.2298/PAC1601001P.

[39] Wu X, Lian Q, Li D, Jin Z. Biphasic osteochondral scaffold fabrication using multi-material mask projection stereolithography. Rapid Prototyp J 2019;25:277–88. doi:10.1108/RPJ-07-2017-0144.

[40] Lian Q, Yang F, Xin H, Li D. Oxygen-controlled bottom-up mask-projection stereolithography for ceramic 3D printing. Ceram Int 2017;43:14956–61. doi:10.1016/j.ceramint.2017.08.014.

[41] Wang JC, Dommati H, Hsieh SJ. Review of additive manufacturing methods for high-performance ceramic materials. Int J Adv Manuf Technol 2019;103:2627–47. doi:10.1007/s00170-019-03669-3.

[42] Londoño-Restrepo SM, Jeronimo-Cruz R, Millán-Malo BM, Rivera-Muñoz EM, Rodriguez-García ME. Effect of the Nano Crystal Size on the X-ray Diffraction Patterns of Biogenic Hydroxyapatite from Human, Bovine, and Porcine Bones. Sci Rep 2019;9:1–12. doi:10.1038/s41598-019-42269-9.

[43] Szcześ A, Hołysz L, Chibowski E. Synthesis of hydroxyapatite for biomedical applications. Adv Colloid Interface Sci 2017;249:321–30. doi:10.1016/j.cis.2017.04.007.

[44] Leventouri T. Synthetic and biological hydroxyapatites: Crystal structure questions. Biomaterials 2006;27:3339–42. doi:10.1016/j.biomaterials.2006.02.021.

[45] Rahman SU. Hydroxyapatite and tissue engineering. Handb Ion Substituted Hydroxyapatites 2020:383–400. doi:10.1016/b978-0-08-102834-6.00016-1.

[46] Kattimani VS, Kondaka S, Lingamaneni KP. Hydroxyapatite–-Past, Present, and Future in Bone Regeneration. Bone Tissue Regen Insights 2016;7:BTRI.S36138. doi:10.4137/btri.s36138.

[47] Erbereli R. AVALIAÇÃO DA QUALIDADE ÓSSEA DE BOVINOS. Universidade de São Paulo, 2107.

[48] ASTMF1185-03. Standard Specification for Composition of Ceramic Hydroxylapatite for Surgical 1993;88:1–3.

[49] De Camargo IL, Erbereli R, Taylor H, Fortulan CA. 3Y-TZP DLP additive manufacturing: Solvent-free slurry development and characterization. Mater Res 2021;24:2–9. doi:10.1590/1980-5373-MR-2020-0457.

[50] Ding G, He R, Zhang K, Xia M, Feng C, Fang D. Dispersion and stability of SiC ceramic slurry for stereolithography. Ceram Int 2020;46:4720–9. doi:10.1016/j.ceramint.2019.10.203.

[51] Chen Z, Li J, Liu C, Liu Y, Zhu J, Lao C. Preparation of high solid loading and low viscosity ceramic slurries for photopolymerization-based 3D printing. Ceram Int 2019;45:11549–57. doi:10.1016/j.ceramint.2019.03.024.

[52] Li K, Zhao Z. The effect of the surfactants on the formulation of UV-curable SLA alumina suspension. Ceram Int 2017;43:4761–7. doi:10.1016/j.ceramint.2016.11.143.

[53] Zhang S, Sha N, Zhao Z. Surface modification of α-Al2O3 with dicarboxylic acids for the preparation of UV-curable ceramic suspensions. J Eur Ceram Soc 2017;37:1607–16. doi:10.1016/j.jeurceramsoc.2016.12.013.

[54] Zhang K, Xie C, Wang G, He R, Ding G, Wang M, et al. High solid loading, low viscosity photosensitive Al2O3 slurry for stereolithography based additive manufacturing. Ceram Int 2019;45:203–8. doi:10.1016/j.ceramint.2018.09.152.

[55] Xing H, Zou B, Lai Q, Huang C, Chen Q, Fu X, et al. Preparation and characterization of UV curable Al2O3 suspensions applying for stereolithography 3D printing ceramic microcomponent. Powder Technol 2018;338:153–61. doi:10.1016/j.powtec.2018.07.023.

[56] Zhou M, Liu W, Wu H, Song X, Chen Y, Cheng L, et al. Preparation of a defect-free alumina cutting tool via additive manufacturing based on stereolithography – Optimization of the drying and debinding processes. Ceram Int 2016;42:11598–602. doi:10.1016/j.ceramint.2016.04.050.

[57] Hinczewski C, Corbel S, Chartier T. Ceramic suspensions suitable for stereolithography. J Eur Ceram Soc 1998;18:583–90. doi:10.1016/s0955-2219(97)00186-6.

[58] Camargo, Italo Leite de; Erbereli, Rogério; Lovo, João Fiore Parreira; Fortulan CA. DLP 3D Printer with innovative recoating system. BTSym2020, 2020, p. 1–8.

[59] Camargo, Italo Leite de; Erbereli, Rogério; Lovo, João Fiore Parreira; Fortulan CA. DLP ADDITIVE MANUFACTURING OF CERAMICS : PHOTOSENSITIVE PARAMETERS , THERMAL ANALYSIS , POST-PROCESSING , AND PARTS, 2021.

[60] Ronca A, D'Amora U, Raucci MG, Lin H, Fan Y, Zhang X, et al. A combined approach of double network hydrogel and nanocomposites based on hyaluronic acid and poly(ethylene glycol) diacrylate blend. Materials (Basel) 2018;11. doi:10.3390/ma11122454.

[61] Johansson E, Lidström O, Johansson J, Lyckfeldt O, Adolfsson E. Influence of resin composition on the defect formation in alumina manufactured by stereolithography. Materials (Basel) 2017;10. doi:10.3390/ma10020138.

[62] Sokolov PS, Komissarenko DA, Dosovitskii GA, Shmeleva IA, Slyusar' I V., Dosovitskii AE. Rheological Properties of Zirconium Oxide Suspensions in Acrylate Monomers For Use In 3D Printing. Glas Ceram (English Transl Steklo i Keramika) 2018;75:55–9. doi:10.1007/s10717-018-0028-3.

[63] ASTM C373-18. Standard Test Methods for Determination of Water Absorption and Associated Properties by Vacuum Method for Pressed Ceramic Tiles and Glass Tiles and Boil Method for Extruded Ceramic Tiles and Non-tile Fired Ceramic Whiteware Products 1 2018:1–7. doi:10.1520/C0373-18.2.

[64] ASTMC1424−15. Standard Test Method for Monotonic Compressive Strength of Advanced Ceramics at 2021;i:1–14. doi:10.1520/C1424-15R19.ization.

[65] Ravaglioli, A., Krajewski A. Bioceramics. 1991. doi:10.1007/978-1-84882-664-9_3.

[66] Wu Z, Liu W, Wu H, Huang R, He R, Jiang Q, et al. Research into the mechanical properties, sintering mechanism and microstructure evolution of Al2O3-ZrO2 composites fabricated by a stereolithography-based 3D printing method. Mater Chem Phys 2018;207:1–10. doi:10.1016/j.matchemphys.2017.12.021.

[67] Griffith, Michelle L.; Halloran FW. Freeform Fabrication of ceramics via Stereolithography. J Am Ceram Soc 1996;79:2601–8.

[68] Pfaffinger M, Hartmann M, Schwentenwein M, Stampfl J. Stabilization of tricalcium phosphate slurries against sedimentation for stereolithographic additive manufacturing and influence on the final mechanical properties. Int J Appl Ceram Technol 2017;14:499–506. doi:10.1111/ijac.12664.

[69] Wei Y, Zhao D, Cao Q, Wang J, Wu Y, Yuan B, et al. Stereolithography-Based Additive Manufacturing of High-Performance Osteoinductive Calcium Phosphate Ceramics by a Digital Light-Processing System. ACS Biomater Sci Eng 2020;6:1787–97. doi:10.1021/acsbiomaterials.9b01663.

[70] Sudan K, Singh P, Gökçe A, Balla VK, Kate KH. Processing of hydroxyapatite and its composites using ceramic fused filament fabrication (CF3). Ceram Int 2020;46:23922–31. doi:10.1016/j.ceramint.2020.06.168.

[71] Yao Y, Qin W, Xing B, Sha N, Jiao T, Zhao Z. High performance hydroxyapatite ceramics and a triply periodic minimum surface structure fabricated by digital light processing 3D printing. J Adv Ceram 2021;10:39–48. doi:10.1007/s40145-020-0415-4.

[72] Misch CE, Qu Z, Bidez MW. Mechanical properties of trabecular bone in the human mandible: Implications for dental implant treatment planning and surgical placement. J Oral Maxillofac Surg 1999;57:700–6. doi:10.1016/S0278-2391(99)90437-8.

[73] Lim HK, Hong SJ, Byeon SJ, Chung SM, On SW, Yang BE, et al. 3D-printed ceramic bone scaffolds with variable pore architectures. Int J Mol Sci 2020;21:1–12. doi:10.3390/ijms21186942.